Journal of
Synchrotron Radiation
ISSN 0909-0495
Editors: **G. Ice, Å. Kvick and T. Ohta**

Coherent X-ray diffraction investigation of twinned microcrystals

Miguel A. G. Aranda, Felisa Berenguer, Richard J. Bean, Xiaowen Shi, Gang Xiong, Stephen P. Collins, Colin Nave and Ian K. Robinson

J. Synchrotron Rad. (2010). **17**, 751–760

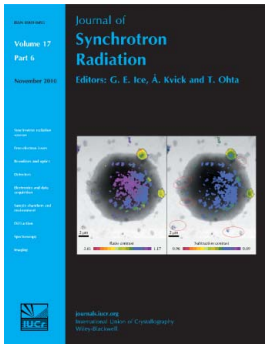

Journal of
Synchrotron Radiation

ISSN 0909-0495

Received 23 August 2010
Accepted 5 October 2010

Coherent X-ray diffraction investigation of twinned microcrystals

Miguel A. G. Aranda,[a]* Felisa Berenguer,[b] Richard J. Bean,[b] Xiaowen Shi,[b] Gang Xiong,[b] Stephen P. Collins,[c] Colin Nave[c] and Ian K. Robinson[b,c]*

[a]Departamento de Química Inorgánica, Cristalografía y Mineralogía, Universidad de Málaga, 29071 Málaga, Spain, [b]London Centre for Nanotechnology, University College, 17–19 Gordon Street, London WC1H 0AH, UK, and [c]Diamond Light Source Ltd, Diamond House, Harwell Science and Innovation Campus, Didcot, Oxfordshire OX11 0DE, UK. E-mail: g_aranda@uma.es, i.robinson@ucl.ac.uk

Coherent X-ray diffraction has been used to study pseudo-merohedrally twinned manganite microcrystals. The analyzed compositions were $Pr_{5/8}Ca_{3/8}MnO_3$ and $La_{0.275}Pr_{0.35}Ca_{3/8}MnO_3$. The prepared loose powder was thermally attached to glass (and quartz) capillary walls by gentle heating to ensure positional stability during data collection. Many diffraction data sets were recorded and some of them were split as expected from the main observed twin law: 180° rotation around [101]. The peak splitting was measured with very high precision owing to the high-resolution nature of the diffraction data, with a resolution ($\Delta d/d$) better than 2.0×10^{-4}. Furthermore, when these microcrystals are illuminated coherently, the different crystallographic phases of the structure factors induce interference in the form of a speckle pattern. The three-dimensional speckled Bragg peak intensity distribution has been measured providing information about the twin domains within the microcrystals. Research is ongoing to invert the measured patterns. Successful phase retrieval will allow mapping out the twin domains and twin boundaries which play a key role in the physical properties.

Keywords: coherent diffraction; CXDI; pseudo-merohedral twinning; perovskites; manganites.

1. Introduction

Twinning is a crystal growth anomaly in which the specimen is composed of several distinct domains whose orientations are related by one or more symmetry elements that are not a part of the space-group symmetry of the single crystal, *i.e.* related by the so-called twin operator(s) or twin law(s) (Cahn, 1954; Santoro, 1974; Yeates, 1997). Multiple-crystal growth disorders are common, but twinning refers to special cases where the extra symmetry element(s) must be of the kind encountered in crystal morphology (a centre of symmetry, a mirror plane or a rotation axis). If the extra symmetry element is a mirror plane, called a twin plane, then this plane must be parallel to a lattice plane of the same *d*-spacing in both domains. If the extra symmetry is a rotation axis, called a twin axis, then this axis must be parallel to a lattice row common to both domains (Cahn, 1954; Koch, 1992). The twinning occurrence is fairly common in crystals of inorganic materials, organic compounds and macromolecular specimens, and it can be a serious complication in the crystal structure determination process.

Several different categories of twinning can be defined according to the coincidence of the separated lattices (Buerger, 1960; Yeates, 1997). The situation in which the lattice overlap occurs in two (or one) dimensions is known as non-merohedral or epitaxial twinning. The case in which the lattices of the domains coincide exactly in three dimensions is known as merohedral twinning. Hemihedral twinning is a special subclass where there are just two domain orientations. The cases where the lattices overlap approximately, but not exactly, in three dimensions are referred to as pseudo-merohedral twinning. This requires unusual unit-cell geometries that yield a lattice with pseudo-symmetry which is higher than the point-group symmetry (for instance the case of orthorhombic perovskites with $a \simeq c$, both edges deriving from the cubic parent structure).

Perovskite materials display many interesting properties including ferromagnetism, piezo- and ferro-electricity, multiferroic behaviour, *etc*. The archetypal perovskite structure is cubic but, in order to fine-tune the physical properties, structural distortions may take place with many materials being orthorhombic or monoclinic. Low-symmetry perovskite crys-

tals therefore fulfil the requisites for pseudo-merohedry and they are commonly twinned. Twinning in orthorhombic perovskites has been extensively studied by a number of techniques including transmission electron microscopy (TEM) (White *et al.*, 1985; Keller & Buseck, 1994; Hervieu *et al.*, 1996), precession electron diffraction (Ji *et al.*, 2009), photoemission spectroscopy (Sarma *et al.*, 2004), neutron single-crystal diffraction (Daoud-Aladine *et al.*, 2002) and X-ray single-crystal diffraction (Van Aken *et al.*, 2002). Furthermore, $Pr_{0.5}Ca_{0.5}MnO_3$ twinned crystals were studied by synchrotron (micro)diffraction to map the domains (Turner *et al.*, 2008) but the coherence properties of the beam were not fully exploited to provide information about the crystal structure in real space. To the best of our knowledge there are no other reported works dealing with the study of twinned crystals by coherent X-ray diffraction.

Here we apply the method of coherent X-ray diffraction imaging (CXDI), which is a rapidly advancing form of lensless microscopy (Neutze *et al.*, 2000; Vartanyants *et al.*, 2007; Jiang *et al.*, 2008; Thibault *et al.*, 2008; Nishino *et al.*, 2009; Robinson *et al.*, 2010, and references therein) that was opened up by the realisation that oversampled diffraction patterns may be inverted to obtain real-space images. The possibility was first pointed out by Sayre (1952) and demonstrated by Miao *et al.* (1999). The phase information of the diffraction pattern, which is lost in the intensity measurement, is embedded in a sufficiently sampled coherent diffraction pattern, which may allow the inversion of the diffraction data set back to an image by computational methods. In addition to obtaining three-dimensional images of studied nanoparticles, CXDI may give different types of information including the quantitative strain field inside a crystal (Pfeifer *et al.*, 2006; Robinson & Harder, 2009; Newton *et al.*, 2010).

In this paper we focus on the use of CXDI for studying twinned microcrystals. When such a crystal is illuminated coherently, speckle patterns can form owing to the differences in amplitude and/or phase of the structure factors for different twin domains, and also from the continuous phase changes between them. Here, we show that this three-dimensional speckled Bragg peak distribution can be measured providing information about the twin domains within the crystals. Research is ongoing to invert the patterns to obtain three-dimensional images of the twin distribution. Three-dimensional images of the twinned domains can provide information relevant to the properties of materials. An ultimate goal is that, by separating out each component, more accurate diffraction intensities may be obtained which would help in the structure determination process of twinned crystals.

2. Experimental section

Three manganite compositions were synthesized by the ceramic method as previously reported (Collado *et al.*, 2003). The stoichiometries were $Pr_{5/8}Ca_{3/8}MnO_3$, $La_{5/8}Ca_{3/8}MnO_3$ and $La_{0.275}Pr_{0.35}Ca_{3/8}MnO_3$, and they are hereafter abbreviated PCMO, LCMO and LPCMO, respectively. The three samples were characterized by high-resolution laboratory X-ray powder diffraction at room temperature. Powder patterns were collected on a Philips X'Pert Pro MPD diffractometer equipped with a Ge(111) primary monochromator (strictly monochromatic Cu $K\alpha_1$ radiation) and an X'Celerator detector. Transmission electron microscopy characterization was carried out using a Philips CM-200 microscope with the powders dispersed on copper grids.

The sample preparation step for a CXDI experiment is important as the positional stability of the particles within the beam must be ensured. In order to carry out this type of experiment for loose powders, we have developed a simple method which is valid for thermally stable samples. Dispersed crystals were attached to borosilicate glass (and also quartz) capillaries by gentle heating in a butane flame (using a cigarette lighter) up to the point where the capillary glass softens. The results are better when the heating is applied to vertically arranged capillaries (as horizontally aligned capillaries are prone to severe bending). Fig. 1 shows an optical microphotograph of a borosilicate glass capillary with the PCMO loose powder thermally attached to the wall.

Coherent X-ray diffraction patterns for selected manganite microcrystals were collected at beamline I16, Diamond Light Source, which is equipped with a six-circle kappa goniometer at 50 m from the source. The wavelength, λ = 1.55 Å (E = 8.00 keV), was selected using a Si(111) channel-cut monochromator. The beam was horizontally focused down to $\sim$4 µm by using a Kirkpatrick–Baez (KB) mirror pair. The vertical and horizontal dimensions of the beam before these mirrors, $\sim$30 µm, were selected by the final beamline slits before the KB mirrors; these slits are not very precise, however. To ensure this beam was reasonably coherent, a 300 µm horizontal slit was placed in front of the beamline focusing mirror (which remained in place in the beamline). This slit is located 27 m from the source and the diffractometer is at 50 m. The horizontal coherence length at the sample is therefore increased to $\lambda D/d$ = 12 µm, assuming stochastic illumination of the intermediate 27 m slit. The sample was aligned by scanning the X-ray absorption of the capillary with a point detector. After the alignment of the capillary, the appropriate Bragg peaks, for instance (121) at 33.17° 2θ for PCMO, were identified by using a Pilatus 100K detector

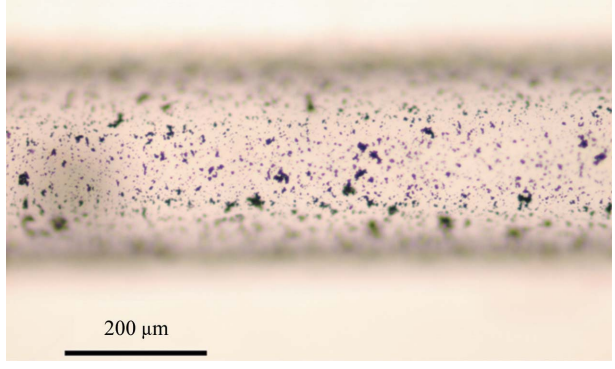

Figure 1
Optical microphotography of dispersed PCMO microcrystals attached to a glass capillary (diameter = 0.3 mm).

(172 μm × 172 μm pixel-size photon counting detector) permanently mounted in the detector arm. After centring the reflection, this detector was moved away and the reflection was again centred in a Princeton Instruments CCD detector with optical coupling to a columnar CsI scintillator. The pixel size was 20 μm × 20 μm and it was placed far from the sample, at 1220 mm, to provide data with sufficient angular resolution. Two-dimensional slices were recorded as the Bragg peak was rocked through the Ewald sphere by rotating the sample within the beam, usually in 0.005° step size (η rocking angle) for about 0.6° although this number depends upon the width of the analyzed peak which was previously pre-scanned at lower resolution. For every discussed scan, the exposure time, number of accumulations and maximum intensity is given below. Coherent diffraction patterns were obtained by collating the slices of the high-resolution scan to form complete three-dimensional diffraction data sets. The pixel binning size and rocking step size were chosen to ensure at least three pixels per fringe, to ensure the data were oversampled.

The coherence of a beam of light is generally described by two components, the transverse and longitudinal coherence lengths, ξ_T and ξ_L, respectively (Born & Wolf, 1999; Leake *et al.*, 2009). The transverse coherence is dependent on the size (S) of the source/undulator itself, and it is given by $\xi_T = \lambda D/S$, where D is the distance from the source to the sample. For a typical third-generation synchrotron beamline, the raw transverse coherence is ∼10 μm and ∼100 μm for the horizontal and vertical directions, respectively. By closing the beamline mid-point slit (see above), the horizontal transverse coherence length was raised to ∼12 μm, sufficient to give some limited degree of coherence beyond the ∼30 μm sample slits. On the other hand, the longitudinal coherence is dependent on the bandwidth of the monochromator, $\xi_L = \lambda^2/2\Delta\lambda$. For a silicon (111) monochromator, $\xi_L \simeq 0.6$ μm. This couples to the optical path length difference of rays through the sample. Therefore, when the crystal size is smaller than the coherence lengths, the sample is said to be in the coherent limit and it meets the required conditions for CXDI measurements. The fringe visibility can be lost by violation of any of the three coherence requirements.

3. Results

Laboratory powder diffraction data for the three manganite samples showed that they were microcrystalline single phase powders. The three phases were indexed in an orthorhombic distorted unit cell of *Pnma* symmetry, with edges $\simeq \sqrt{2}a_c \times 2a_c \times \sqrt{2}a_c$ where a_c stands for the basic perovskites cubic unit-cell parameter, in agreement with previous results (Uehara *et al.*, 1999; Collado *et al.*, 2003). The unit-cell values for the three phases are given in Table 1. It is clear from the unit-cell edges given in Table 1 that these manganites are very prone to pseudo-merohedral twinning.

The sizes, shapes and variability of the manganite particles were studied by TEM. Fig. 2 displays bright and dark field microphotographs for selected particles of PCMO. It must be noted that the dispersion in particle sizes is large, from small particles of about 0.2 μm to large particles longer than 1 μm. The shapes were also variable but most of the observed particles were elongated prisms (see Fig. 2).

Table 1
Unit-cell parameters for $Pr_{5/8}Ca_{3/8}MnO_3$, $La_{0.275}Pr_{0.35}Ca_{3/8}MnO_3$ and $La_{5/8}Ca_{3/8}MnO_3$ determined by X-ray powder diffraction with a laboratory source.

	PCMO	LPCMO	LCMO
a (Å) (a_c)	5.443 (3.849)	5.441 (3.848)	5.448 (3.853)
b (Å) (a_c)	7.676 (3.838)	7.676 (3.838)	7.694 (3.847)
c (Å) (a_c)	5.421 (3.834)	5.440 (3.847)	5.462 (3.863)
S_{ac} (%)	+0.41	0.02	−0.26
$\Delta\alpha_{ac}$ (°)	0.232	0.011	0.147
$\Delta 2\theta_{(200)}$ (°)	0.140	0.010	0.091

Fig. 3 shows the diffraction signal of PCMO and LPCMO microcrystals, collected in the Pilatus detector, as an example. Only those well shaped rounded reflections isolated from any other diffracting signal were centred, for instance the (210) reflection of LPCMO in Fig. 3(*b*).

Three main types of coherent diffraction data sets were recorded on the CCD: (i) single centred, (ii) doubled-centred and (iii) multi-centred peaks. Fig. 4 (top) shows an example of each type of data set as two-dimensional slides. The angles used for the discussion of the results (see below) are also shown in Fig. 4(*b*). Fig. 4 (bottom) displays views of the three-dimensional integrated patterns for the three types of microcrystals in order to highlight the widths of the measured diffraction peaks. Eleven good quality data sets were collected for PCMO and four data sets for LPCMO. It must be high-

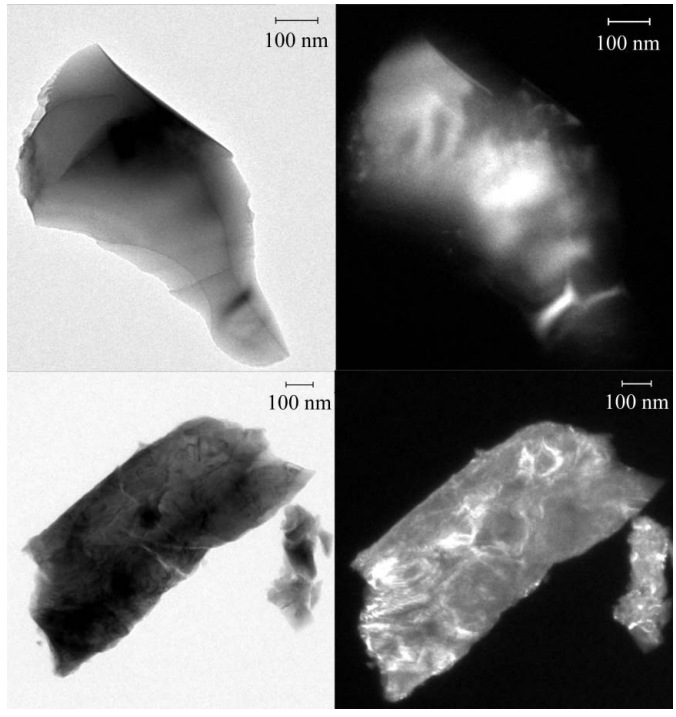

Figure 2
TEM bright (left) and dark (right) field micrographs showing two selected particles of PCMO.

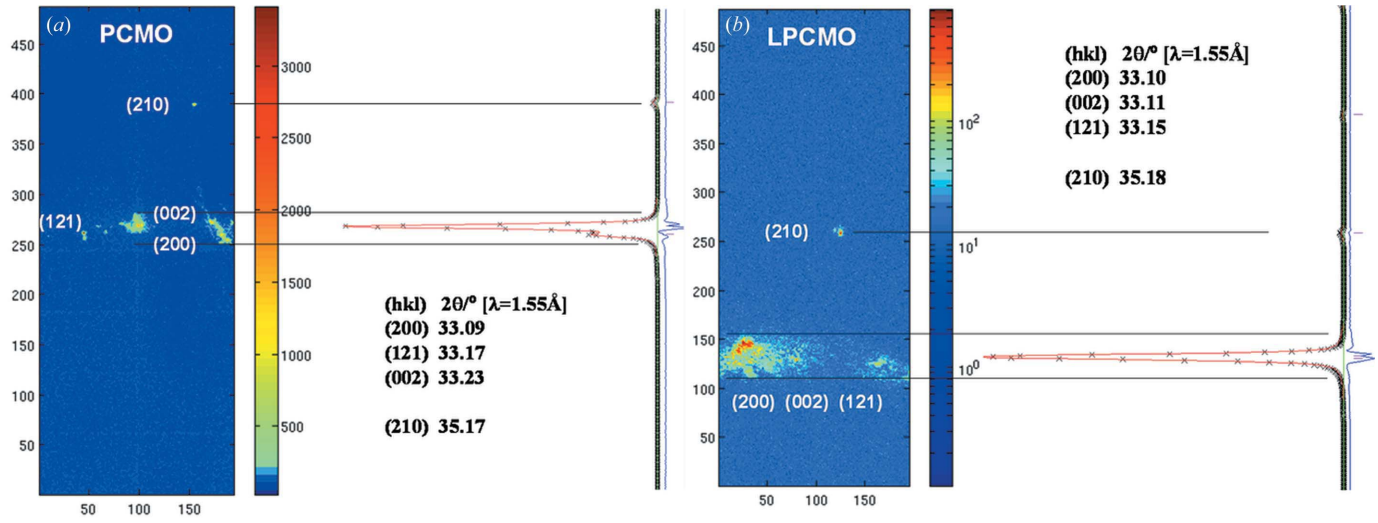

Figure 3
Microcrystal two-dimensional diffraction images of PCMO (*a*) and LPCMO (*b*) collected on the Pilatus detector. The Rietveld-fitted powder diffraction patterns of the corresponding regions are also shown to highlight the width of the regions where diffraction is expected.

lighted that we could not collect CXD data for any of the LCMO microcrystals we tried. The diffraction signal disappears from the CCD detector when centring the crystal. We speculate that the photoelectric effect may be playing an important role as this is the highest electrically conducting sample. Therefore, LCMO will not be further discussed in this work.

4. Real-space phase model of twinning

PCMO has orthorhombic space group *Pnma*, with lattice constants given in Table 1, which is a supercell of the simple cubic perovskite. These perovskites are known to show three main laws for pseudo-merohedral twinning: a 180° rotation around [101], 90° around [101] and a 180° rotation around [121] (Wang & Liebermann, 1993; Keller & Buseck, 1994). The '*a*–*c*' twinning arises from the accommodation of the small difference between the *a* and *c* lattice constants, possibly forming upon cooling the crystals from a higher symmetry phase at elevated temperature. Fig. 5 shows an exaggerated view of the matching of the {101} planes at the twin boundary, running up the figure. It is clear that the *a*–*c* lattice difference corresponds to a small rotation of the twin domains, giving two sets of Bragg peaks for all reflections except along the *hkh* symmetry axis.

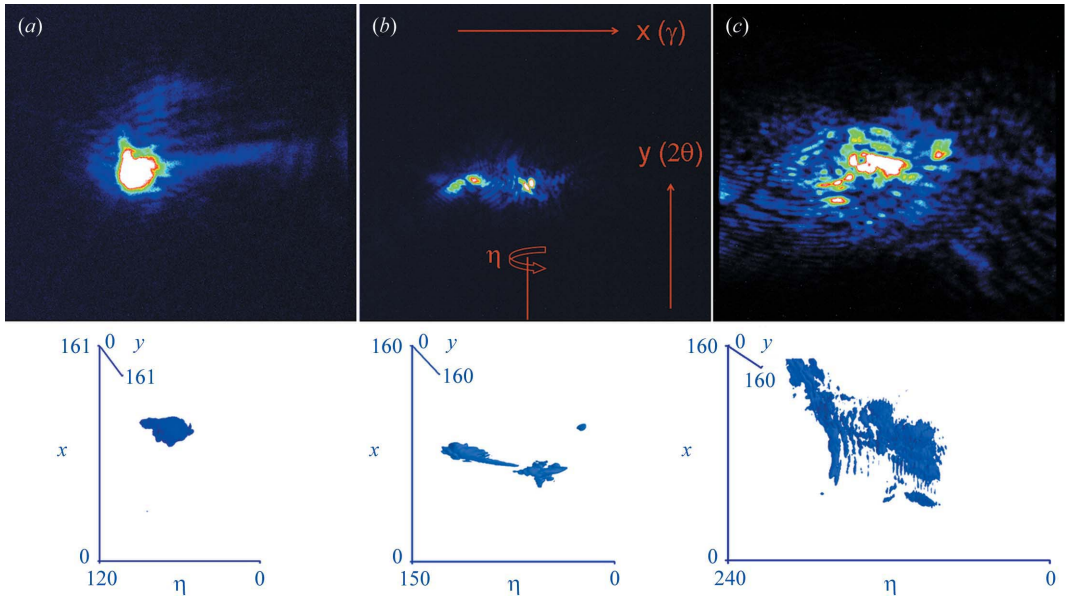

Figure 4
(Top) Coherent diffraction patterns of PCMO crystals showing a single peak with fringes (PCMO1–9, frame 77; 30 s of exposure time, one accumulation, I_{max} = 34600 counts s^{-1}) (*a*), a split Bragg peak with speckles extending between the two centres (PCMO3–7, frame 28; 5 s of exposure time, three accumulations, I_{max} = 71630 counts s^{-1}) (*b*) and a multi-centred data set (PCMO2–13, frame 88; 30 s of exposure time, one accumulation, I_{max} = 4260 counts s^{-1}) (*c*). The full CCD recording area is shown for the sake of comparison. The angles discussed in the paper (η, γ and 2θ) are also displayed. (Bottom) Projections of the three-dimensional 'collated' diffraction patterns showing the overall widths of the diffraction peaks.

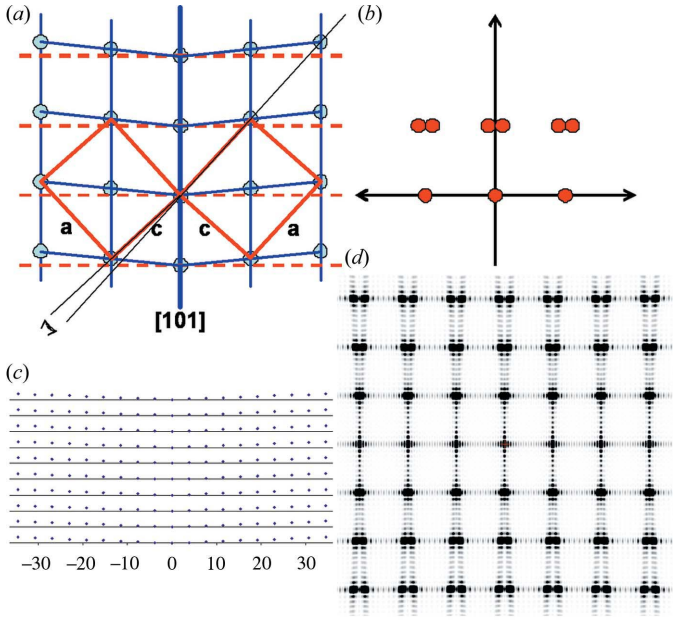

Figure 5
(*a*) Exaggerated schematic view of a pseudo-merohedral twin pair owing to 180° rotation around [101] for orthorhombically distorted perovskite. (*b*) Calculated diffraction spots illustrating the splitting of the Bragg peaks. (*c*) Two-dimensional model of the two domains, each containing 9 × 9 unit cells, with the difference between the *a* and *c* dimensions being ten times greater than is the case for the PCMO crystals in order to magnify the effects for demonstration purposes. (*d*) Calculated scattering pattern using the *nearBragg* program from the two-dimensional twinned crystal given in (*c*).

If the domains are small, their Bragg peaks will be enlarged owing to the classical 'finite size' effect. If the domains are sufficiently small, the two members of the split Bragg peaks will overlap and, assuming the beam is coherent over the size of the domains, will lead to interference effects in the overlap region of the diffraction pattern. Each of the two peaks will be speckled owing to the domain arrangement within the illuminated piece of crystal and the speckles will combine together in the interference pattern. It is a general rule, for domain structures at least, that the number of speckles in the peak is approximately equal to the number of domains in the beam. The rule assumes the domains are independent, with large phase shifts between them, and applies in one, two or three dimensions. The rule can be derived by noting that the size of a speckle is the reciprocal of the size of the illuminated area, while the width of the speckle distribution is the reciprocal of the size of a typical domain.

The words 'speckle' and 'fringe' are used rather interchangeably in the literature. Fringes appear in optical interferometers as regular linear arrays of constructive and destructive interference, and are used as a way to measure coherence, among other things. Fringes also arise in the shape-diffraction patterns of simple objects, parallel from pairs of edges or circular from round apertures or scatterers. Speckles, on the other hand, are the result of random interference between a large number of waves with arbitrary, yet well defined, amplitudes and phases. In principle their degree of modulation can be used to measure coherence, as reported by Alaimo *et al.* (2009) using the dynamical near-field speckles formed by scattering from colloidal particles. The inherently random nature of domain structures owing to twinning are therefore expected to give rise to speckles rather than simple fringes. Here, we use the term 'speckle' to describe the fluctuation in the Bragg peak intensity distribution owing to interference between the (smaller) twin domains, and the term 'fringe' to mean the structure owing to the (larger) crystallites. If the domain structure exists across the entire crystal, the spacing between the speckles will be determined by the crystal size. However, the overall peaks will have a breadth dependent on the domain size with the number of speckles in the peak related to the number of domains in the crystal. The formation of both speckles and fringes is a necessary consequence of having some degree of coherence in the beam.

There is considerable merit, where possible, in modelling the diffracting object as the product of a periodic structure (the ideal crystal) and a macroscopic modulation of the phase that characterizes the structures of interest (*i.e.* twin domains). In reciprocal space, such a multiplication becomes a convolution, and the motif of the macroscopic object is repeated around each point in reciprocal space. In the present case, such a treatment is complicated by the presence of two lattices. We would like to interpret the combined double Bragg peak, along with these speckles, in terms of the Fourier transform of a single object in real space. We therefore make use of the shifting property of the Fourier transform: when the object in real space is multiplied by a linear phase ramp, the diffraction pattern is shifted by an amount proportional to the ramp. In this way the two Bragg peaks of the split pair, shifted in opposite directions, can be attributed to separate regions of the crystal overlaid with opposite-directed phase ramps. This is illustrated in Fig. 5(*a*), where the independent lattices of the two separate domains can be described as a transformation from a single reference lattice. If the origin is chosen at the corner of the unit cells meeting at the twin plane, each unit cell is shifted by an amount proportional to its distance from the twin plane, or a linear function of its distance. This shift gives rise to a phase in the diffraction that increases linearly with distance from the twin plane, in other words a phase ramp. Therefore, through the Fourier shift theorem, the two domains give rise to opposite peak shifts in the combined diffraction pattern, seen as the splitting.

This picture is easily generalized to the full mosaic domain structure of an arbitrarily twinned crystal, which is thereby mapped onto a complex image of unit amplitude and spatially varying phase. All the left-rotated domains have phase ramps with negative slope and all the right-rotated domains have phase ramps with positive slope; where they join, the phase should be continuous (although their derivatives are not), assuming they meet at a complete unit-cell boundary, but the slope reverses. The picture can be readily generalized to three dimensions: the macroscopic real-space phase is simply the three-dimensional displacement of the atoms from those of the ideal reference lattice, projected onto the Q-vector of the reflection under consideration. The choice of 'reference'

lattice is arbitrary; it simply defines the reciprocal lattice with respect to which the peak shifts are observed.

The program *nearBragg* (http://bl831.als.lbl.gov/~jamesh/nearBragg/) from James Holton was used for some initial simulations. The following description is extracted from the *nearBragg* manual: "...*nearBragg* calculates the distance from one or more source points to each 'atom' and then from the 'atom' to the centre of a detector pixel. The sin and cos of 2π times the number of wavelengths involved in this total distance is then added up and the amplitude and phase of the resultant wave from the whole sample (and the whole source) are obtained for each pixel. The intensity at each pixel is the modulus-square of the amplitude. The atoms are considered point scatterers with an intrinsic structure factor of '1' in all directions...". Results from one of the simulations are shown in Fig. 5(*d*). This type of simulation is easy to relate to the schematic in Fig. 5(*a*) and it is shown for this reason. However, the phase ramp description gives the same results [as will be shown below in Fig. 6(*a*)] and it is computationally much faster for three-dimensional objects. The phase ramp description is therefore used for the remaining simulations.

To illustrate the effect of the opposite phase ramps on the diffraction patterns, in Fig. 6 we present two simulated three-dimensional objects with a double phase ramp. The calculations are carried out using a fast Fourier transform on a 256 × 256 × 128 array and an object of 48 × 24 × 24 grid points, such that each simulated twin domain has a cubic shape. The amplitudes are 1 within the object and 0 outside. The introduced phase ramps within the object are shown on a colour wheel with green representing $\varphi = 0$, blue $\varphi = -\pi$ and red $\varphi = +\pi$. The corresponding amplitudes of the three-dimensional diffraction pattern are depicted at the bottom of the figure showing the splitting of the peak owing to the phase structure and the intermodulation of the diffraction in between. The magnitude of the ramps, 1.5π and 2π, in Figs. 6(*a*) and 6(*b*), respectively, corresponds to an increasing angular separation of the peaks (see Fig. 6, bottom). Since the fringe spacing is fixed by the crystal size, the result is an increasing number of fringes connecting the two centres of the Bragg peaks as the slope of the ramps increases (Fig. 6*b*).

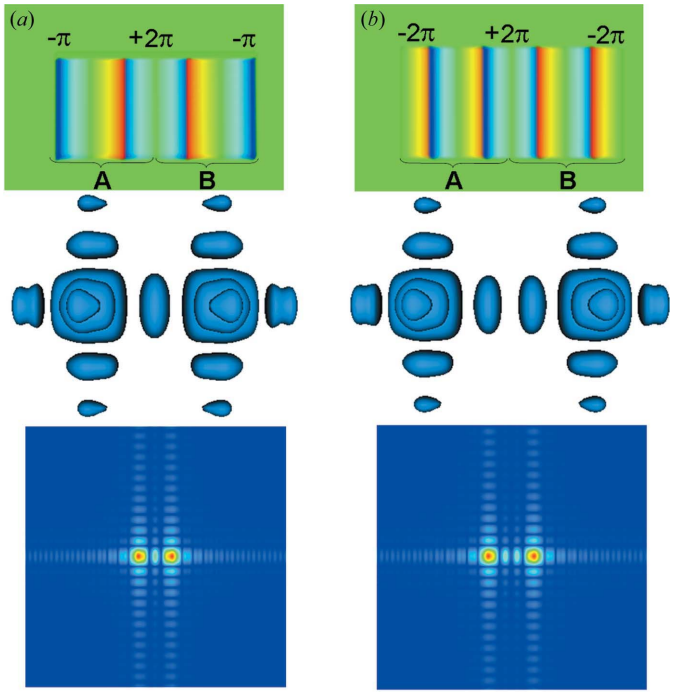

Figure 6
(Top) Two bicrystals shown as a translucent three-dimensional box with colours representing the phase change. The two twins (*A* and *B*) have the same dimension (24 × 24 × 24 grid points) but different slopes of the phase ramps: (*a*) 1.5π, (*b*) 2π. (Middle) Calculated three-dimensional coherent diffraction patterns of the two twinned objects. (Bottom) Isoscalar plane cut of the diffraction patterns.

So far we have omitted the structure factor from this discussion, but it is straightforward to introduce that too. In the perovskite case we have been considering that the two member peaks of the pair will have roughly the same structure factor, even if they have different indices, because they are attributed to the same reflection of the cubic parent structure. In the general case where different unrelated structure factors mix together, this must be built into the complex object whose Fourier transform gives the full diffraction (speckle) pattern. Both the amplitude and phase of the structure factor are attributed to the regions of space occupied by the domain, multiplied by the phase ramp function corresponding to the domain rotation relative to the reference lattice. This picture applies equally to the interpretation of data: following phase retrieval of the diffraction pattern, the inverted three-dimensional image of the crystal can be interpreted directly in terms of local structure factors and domain rotations (ramps).

It is known that phase retrieval is difficult in this general case and methods still need to be developed. The best methods to date, based on Fienup's (1982) 'hybrid input–output' method, still require a 'real-space constraint'. The description above could conceivably be coded into a suitable algorithm, for example exploiting the slow-varying continuous property of the real-space phase image. Such a method has been used successfully by Minkevich *et al.* (2007) for analysing strains in semiconductor heterostructures (without twinning).

However, if phase retrieval and imaging are not possible, limited information can be extracted from the diffraction pattern itself. The speckle contrast, usually defined as the 'visibility' $(I_{\max} - I_{\min})/(I_{\max} + I_{\min})$, is a rough estimate of the range of real-space phases present in a diffracting object. If the object is a pure, but weak, phase object, illuminated by a soft-edged beam, then it can be shown, by a vector summation diagram representing the Fourier transform, that the speckle contrast is proportional to the range of phases present in the object, envisaged as a real-space phase map in three dimensions. The speckle contrast can be estimated experimentally as the variance of the intensity over parts of the diffraction pattern. There is a potentially important application to the case of merohedral twinning discussed above. When domains of different structure factor but identical lattice are present in a twinned crystal, the speckle visibility will be proportional to the crystallographic (complex) amplitude difference between the two structure factors. This might have some potential in crystallographic phase measurement. In other cases, the

speckle contrast will be due to internal grain boundaries (density discontinuities) within the sample. For pseudo-merohedral twinning, each component of the split Bragg peak receives its main contribution from domains with only one of the two orientations. These domains might be separated from each other by 'unseen' domains with the alternative orientation, an extreme example of a density discontinuity. This is the probable reason why a relatively high speckle contrast is observed for the manganites studied here.

The important result of this section is that we can represent the complicated array of twin domains within a crystal, in which the lattice is separately defined for each domain, in terms of a phase field over the entire object. The relative positions of the domains are mapped onto phase shifts, while the local rotations are mapped onto phase ramps. This method is generally applicable, but might have little useful meaning in the limit of very small domains or the case of partially crystalline or amorphous materials.

5. Discussion

Firstly, the data shown in Fig. 3, which are representative of many recorded images, deserve a brief discussion. PCMO, as shown in Table 1, has a much larger orthorhombic *ac* distortion than LPCMO. This may be quantified by the lattice strain in the *ac* plane, S_{ac} (%),

$$S_{ac} = \frac{2(a-c)}{(a+c)} \times 100, \qquad (1)$$

and the corresponding values are given in Table 1. The larger distortion for PCMO is also evident in Fig. 3 as the (200) and (002) Bragg reflections are partially resolved in the powder diffraction pattern. For LPCMO, those reflections are not resolved in the powder pattern, owing to the very low orthorhombic distortion, but some studied microcrystals showed very large peak widths. The data shown in Fig. 3 for LPCMO are indicative of a very large unit-cell parameter distribution for some microcrystals. This may be due to inhomogeneities in the cation distribution of this solid solution but it may also be due to large microstrain owing to the rich twin structure of these compositions. This observation may be much related to its very complex low-temperature behaviour displaying mesoscopic phase separation (Uehara *et al.*, 1999) and persistent magnetoresistive memory effect (Levy *et al.*, 2002).

Now we discuss the results obtained in the coherent high-resolution diffraction patterns. We will focus on split Bragg reflections and we will not consider in this work the unsplit peaks as they are not likely to arise from twinned regions of the manganite microparticles. Most of this study was dedicated to recording data around the $2\theta \simeq 33.1^\circ$ region as it contains the most intense diffraction peaks of these manganites: (200), (121) and (020) (see Fig. 3). It must be noted that these reflections cannot be distinguished by their measured 2θ values as they have almost the same *d*-spacings, with their angular positions slightly dependent upon the centring of the microcrystal in the beam. However, their splitting behaviour owing to the *ac* twinning is quite different (see Fig. 5).

Firstly, let us consider a (121) reflection. The 2θ Bragg angle for the pair arising from the two twin domains must have the same value but they will be rotated by an angle, $\Delta\alpha_{ac}$, defined as

$$\Delta\alpha_{ac} = (\pi/2) - 2\tan^{-1}(a/c) \quad \text{or} \quad \Delta\alpha_{ac} \simeq 1 - a/c. \qquad (2)$$

The theoretical values for this splitting angle are also given in Table 1. For PCMO, we have collected three data sets with split peaks with an average $\Delta\alpha_{ac}$ value of 0.23 (1)°, which were measured from the diffraction data as detailed in equation (3) (see Fig. 4*b*),

$$\Delta\alpha = \left(\Delta\eta^2 + \Delta\gamma^2\right)^{1/2}. \qquad (3)$$

This value is in excellent agreement with the expected angle between the axes of the two twin individuals (see Table 1). It must be noted that the measured 2θ angles for two centres were the same for this type of reflection. An example of this type of double-centred coherent diffraction data set is shown in Fig. 4(*b*). This misfit angle has been previously reported (see, for instance, Wang & Liebermann, 1993) but the value was larger (~1°) because the lattice strain in the *ac* plane for the studied natural perovskites, $CaTiO_3$, is larger.

Secondly, let us consider a (200) [or (002)] type reflection. It is clear that, for a single domain crystal, if one reflection is observed on the detector the other cannot be measured as it is perpendicular. However, when the (200) reflection of a pseudo-merohedrally twinned microcrystal is being measured, the (002) diffraction from the other twin domain will also be present close to that diffraction angle. The 2θ difference between the two centres of the peaks will be given by the difference in the *d*-spacing values of those planes. So, for the (200)/(002) peaks, we can define $\Delta 2\theta_{(200)}$ which will be the difference of the diffraction angles of the (200) and (002) twin-related diffraction peaks. The values of this angle, for the studied manganite compositions, are also given in Table 1. The angle has been measured for two PCMO microcrystals just by converting the Δy pixel distance to 2θ angle, see Fig. 4(*b*) (using the sample-to-detector distance). Fig. 7(*a*) shows one example of this type of reflection, and the measured $\Delta 2\theta_{(200)}$ angle, 0.15°, is in very good agreement with the expected one, 0.14° (see Table 1). Furthermore, these centres are also displaced in η and γ angles (see Fig. 4*b*). We can determine the $\Delta\alpha_{(200)}$ angle, 0.106°, which was also in very good agreement with the expected one, $(1 - a/c)/2 = 0.116^\circ$.

Furthermore, the (200)/(002) splitting described just above can be generalized to any reflections having $h \neq l$ indexes. We were able to collect coherent diffraction data for a (weak) high-order reflection (220) diffracting at 40.86° (2θ). Fig. 7(*b*) shows one slide of the diffraction data set revealing the (220)/(022) double peak owing to pseudo-merohedral twinning. The measured $\Delta 2\theta_{(220)}$ angle, 0.15°, is relatively close to the expected one, 0.12°. Furthermore, the measured $\Delta\alpha$ angle between the two centres, 0.11°, is also fully consistent with the twin description. Finally, it must be noted that curved fringes

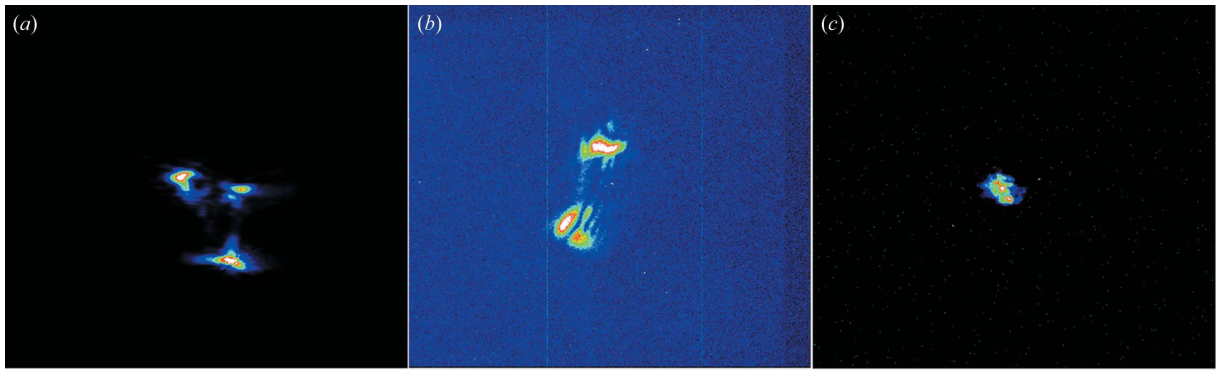

Figure 7
Coherent diffraction images for (*a*) (200)/(002) twin pair (PCMO1–18, frame 21; 2 s of exposure time, five accumulations, I_{max} = 327670 counts s^{-1}), (*b*) (220)/(022) twin pair (PCMO3–4, frame 33; 120 s of exposure time, one accumulation, I_{max} = 2330 counts s^{-1}) and (*c*) likely (200)/(002) twin pair (LPCMO16, frame 43; 60 s of exposure time, one accumulation, I_{max} = 2440 counts s^{-1}). Note the curved fringes that connect both twin peaks in (*b*). The full CCD recording area is shown for the sake of comparison.

connecting the two peak centres, see Fig. 7(*b*), were also observed in other coherent X-ray diffraction data sets.

The consequences of twinning in the diffraction data sets described above are also applicable to LPCMO microcrystals. However, to distinguish between (121) and (200) type reflections is not straightforward because the very low S_{ac} lattice difference (see Table 1) makes the peak splitting very small for both type of reflections. For LPCMO microcrystals, five data sets were measured and two of them have clear split peaks. Fig. 7(*c*) shows an image of a split peak. The measured $\Delta 2\theta_{(200)}$ angle, 0.022°, is larger than the expected value, 0.010° (see Table 1). The measured $\Delta\alpha$ angle between the two centres was 0.057°. Although the split angles are somewhat larger that the expected ones, for the average composition, these observations are totally consistent with this twin description. Furthermore, this is to be expected because the (average) composition of the studied microcrystal may be not exactly the same as that of the powder.

Since the beam was made coherent during the experiment by use of a coherence-defining aperture and then focused to obtain sufficient intensity from the micrometre-sized crystals, the speckles and fringes of the diffraction patterns of split Bragg peaks were found to interfere with each other and give a single merged coherent diffraction pattern. From the fringes spacing, an estimation of the crystal sizes can be made,

$$\text{Size (nm)} \simeq \lambda D/np_s \simeq 9455/n, \qquad (4)$$

where D is the sample-to-detector distance, n is the average number of the pixel for the repeating fringes, and p_s is the pixel size of the CCD detector. We have applied equation (4) to many fringe sets such as those shown in Figs. 4 and 7. The average sizes ranged between 450 and 900 nm for different microcrystals. Sizes close to 700 nm were obtained very frequently. These sizes are consistent with those observed by electron microscopy (Fig. 2). It must also be noted that non-regular fringe spacing has been observed for several crystals. This could be due to very strained crystals as reported previously (Cha *et al.*, 2010).

It was observed that the split peaks, discussed above, have different intensities. This can be explained by smaller or fewer domains for one orientation. In order to study the possible effects of the twin domain size, several simulations have been carried out. Fig. 8 displays the three-dimensional coherent diffraction patterns of three twinned objects modelled as explained above. Fig. 8(*a*) displays the pattern for a twin pair with a twin being half the size of its sister. Fig. 8(*b*) displays a similar study but for a twin being four times smaller. Finally, Fig. 8(*c*) shows the simulation for a twin being eight times smaller than its sister. The phase ramp for these simulations is the same as that employed in Fig. 6(*a*). The centre of symmetry evident in Fig. 6 is lost, as expected, because the twins have different sizes but the intermodulation signal between the two peaks is retained. Furthermore, the diffraction peaks arising from the twins with the smaller sizes are wider. As the domain size decreases, with respect to its twin sister, its fringe spacing becomes broader (see Fig. 8*c*) as, with only one domain of each type, the fringe spacing is determined by the size of the domains. This might be an alternative explanation for non-regular fringe spacing.

In addition to the different size of the twin domains, complex strain patterns may take place within the twinned microcrystals. A TEM study of this work (see Fig. 2) and many other reports about these types of manganites (see, for instance, Uehara *et al.*, 1999; Fäth *et al.*, 1999; Kim *et al.*, 2000) showed very complex microstructures and behaviours. The coherent diffraction patterns showed a curved set of fringes [see, for instance, Fig. 7(*b*)] and fringe branches without a constant spacing. In order to justify these observations, we have carried out simulation studies imposing a more complex phase change within the particles. Fig. 9 shows three examples of this type of simulation. In this case the phase is not constant with respect to the faces of the microcrystal but they have a curvature modelled by a parabolic function. The phase ramp is similar to that of Fig. 6(*a*) and the magnitude of the curvature has been varied. As can be seen, Fig. 9(*a*) has a small curvature and its coherent diffraction pattern is quite similar to that reported in Fig. 6(*a*). However, as curvature of the phase

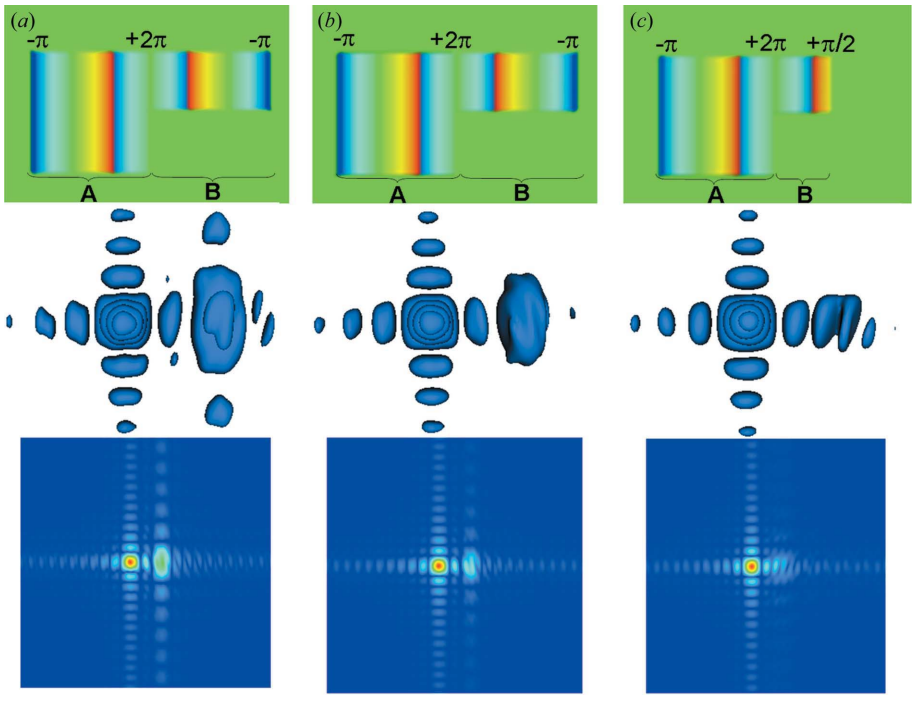

Figure 8
(Top) Three bicrystals shown as a translucent three-dimensional box with colours representing the phase change which is the same as that given in Fig. 6(*a*). The two twins within each bicrystal have different dimensions: (*a*) (24 × 24 × 24) and (24 × 12 × 24), (*b*) (24 × 24 × 24) and (24 × 12 × 12) and (*c*) (24 × 24 × 24) and (12 × 12 × 12) grid points. (Middle) Calculated three-dimensional coherent diffraction patterns of the two twinned objects. (Bottom) Isoscalar plane cut of the diffraction patterns.

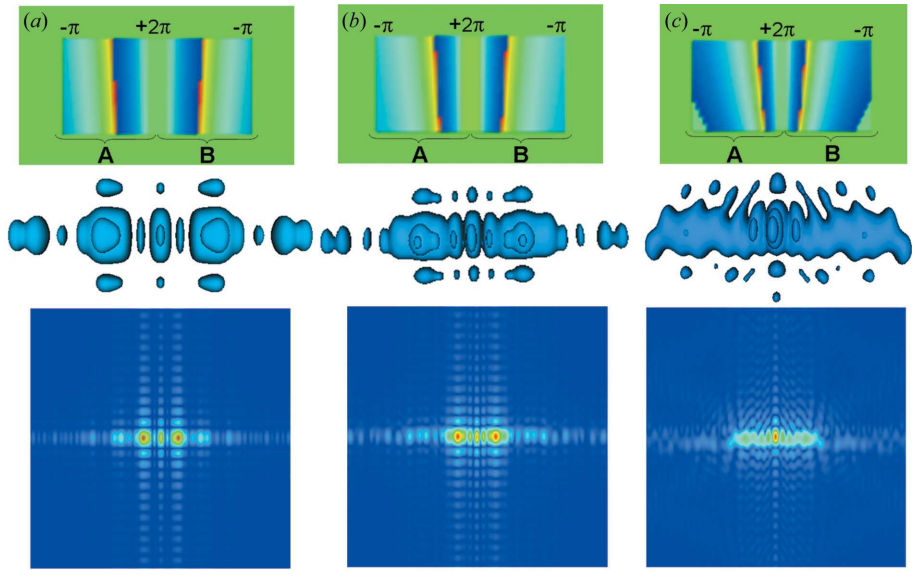

Figure 9
(Top) Three bicrystals shown as a translucent three-dimensional box with colours representing the phase change. The two twins have the same dimension (24 × 24 × 24 grid points) and the same overall variation of the phase ramp. However, the curvature of the parabolic function changes in the three objects. The change has been modelled by displacing the minimum of the parabolic function by 78 (*a*), 35 (*b*) and 15 (*c*) pixels from the object. (Middle) Calculated three-dimensional coherent diffraction patterns of the twinned objects. (Bottom) Selected isoscalar plane cut for the diffraction patterns.

(strain) within the crystal increases (see Fig. 9*b*) the intermodulation signal increases in intensity. Furthermore, when strain is more relevant (see Fig. 9*c*) curvature of the fringes develops. The interplay between non-flat faces, large strain fields and different twin domain sizes is believed to generate the complex fringe/speckle patterns observed in this study.

Finally, simulations were also carried out in order to study the role of the number of domains in the three-dimensional coherent diffraction patterns. Fig. 10 displays the coherent diffraction signal corresponding to a twinned crystal with four alternative domains (*ABAB*). In addition to the split peak, owing to the two types of domains (*A* and *B*), three speckles are evident within each diffraction maxima (see bottom of Fig. 10) for this twin arrangement. The simulations can be interpreted as follows: (i) the number of diffraction peaks is the number of opposite phase ramps (two in this case); (ii) the number of speckles within a peak (three in this case) is the overall number of domains minus one, the speckles within each peak arising from the *ABA* and *BAB* configurations, respectively. This can be readily generalized to *n* domains within a crystal but the diffraction from a given specimen may be complex owing to the possible existence of domains related by different twin laws, not only 180° rotation around [101], and the complex strain pattern within the microcrystal. A multi-twinned microcrystal would give complex three-dimensional patterns such as that shown in Fig. 4(*c*).

In summary, using coherent X-ray diffraction, Bragg peaks of pseudo-merohedral twinned manganite microcrystals have been measured and they were broken up into fringes and speckles. This is consistent with a new theory of the connection between the twinning and the phase of the domain that contributes to a given Bragg peak. It is straightforward to show that the number of speckles in the Bragg peak is indicative of the number of domains in the beam. Our new understanding of the origin of this speckle shows that the visibility is proportional to the phase

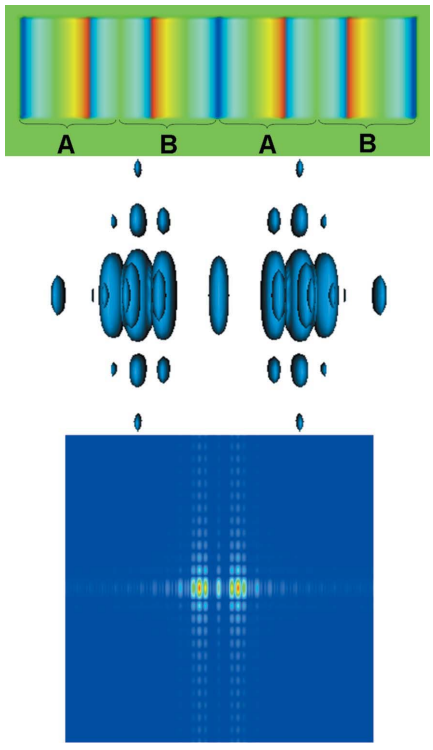

Figure 10
(Top) Twinned crystal with four domains (*ABAB*) shown as a translucent three-dimensional box with the domain dimensions and phase ramps as in Fig. 6(*a*). (Middle) Calculated three-dimensional coherent diffraction pattern. (Bottom) Isoscalar plane cut of the diffraction pattern showing the speckles within the split peaks.

shift between the domains. This method represents an entirely new way of measuring the domains mismatch and it may allow sensitive testing of strain in crystals. In the future, successful phase retrieval will allow mapping out the twin domains and twin boundaries which play a key role in many physical properties like magnetoresistance.

Diamond Light Source is thanked for the provision of X-ray synchrotron diffraction beam time, and Gareth Nisbet for his assistance during the experiment. We also thank James Holton for providing a copy of the *nearBragg* program. The work at Malaga was financed by MAT2009-07016 research grant and at UCL under EPSRC grant EP/F020767/1 and an ERC Advanced grant.

References

Alaimo, M. D., Potenza, M. A. C., Manfredda, M., Geloni, G., Sztucki, M., Narayanan, T. & Giglio, M. (2009). *Phys. Rev. Lett.* **103**, 194805.
Born, M. & Wolf, E. (1999). *Principles of Optics*, 7th ed. Cambridge University Press.
Buerger, M. J. (1960). *Crystal Structure Analysis.* New York: John Wiley and Sons.
Cahn, R. W. (1954). *Adv. Phys.* **3**, 363–445.
Cha, W., Song, S., Jeong, N. C., Harder, R., Yoon, K. B., Robinson, I. K. & Kim, H. (2010). *New J. Phys.* **12**, 035022.
Collado, J. A., Frontera, C., Garcia-Munoz, J. L., Ritter, C., Brunelli, M. & Aranda, M. A. G. (2003). *Chem. Mater.* **15**, 167–174.
Daoud-Aladine, A., Rodriguez-Carvajal, J., Pinsard-Gaudart, L., Fernandez-Dıaz, M. T. & Revcolevschi, A. (2002). *Phys. Rev. Lett.* **89**, 097205.
Fäth, M., Freisem, S., Menovsky, A. A., Tomioka, Y., Aarts, J. & Mydosh, J. A. (1999). *Science*, **285**, 1540–1542.
Fienup, J. (1982). *Appl. Opt.* **21**, 2758–2769.
Hervieu, V., Van Tendeloo, G., Caignaert, V., Maignan, A. & Raveau, B. (1996). *Phys. Rev. B*, **53**, 14274–14284.
Ji, G., Morniroli, J.-P., Auchterlonie, G. J., Drennan, J. & Jacob, D. (2009). *Ultramicroscopy*, **109**, 1282–1294.
Jiang, H., Ramunno-Johnson, D., Song, C., Amirbekian, B., Kohmura, Y., Nishino, Y., Takahashi, Y., Ishikawa, T. & Miao, J. (2008). *Phys. Rev. Lett.* **100**, 038103.
Keller, L. P. & Buseck, P. R. (1994). *Am. Miner.* **79**, 73–79.
Kim, K. H., Uehara, M., Hess, C. & Sharma, P. A. (2000). *Phys. Rev. Lett.* **84**, 2961–2964.
Koch, E. (1992). *International Tables for Crystallography*, Vol. C, edited by A. J. C. Wilson, pp. 10–14. Dordrecht: Kluwer.
Leake, S. J., Newton, M. C., Harder, R. & Robinson, I. K. (2009). *Opt. Express*, **17**, 15853–15859.
Levy, P., Parisi, F., Granja, L., Indelicato, E. & Polla, G. (2002). *Phys. Rev. Lett.* **89**, 137001.
Miao, J., Charalambous, P., Kirz, J. & Sayre, D. (1999). *Nature (London)*, **400**, 342–344.
Minkevich, A. A., Gailhanou, M., Micha, J.-S., Charlet, B., Chamard, V. & Thomas, O. (2007). *Phys. Rev. B*, **76**, 104106.
Neutze, R., Wouts, R., Van der Spoel, D., Weckert, E. & Hajdu, J. (2000). *Nature (London)*, **406**, 752–757.
Newton, M. C., Leake, S. J., Harder, R. & Robinson, I. K. (2010). *Nat. Mater.* **9**, 120–124.
Nishino, Y., Takahashi, Y., Imamoto, N., Ishikawa, T. & Maeshima, K. (2009). *Phys. Rev. Lett.* **102**, 018101.
Pfeifer, M. A., Williams, G. J., Vartanyants, I. A., Harder, R. & Robinson, I. K. (2006). *Nature (London)*, **442**, 63–66.
Robinson, I., Gruebel, G. & Mochrie, S. (2010). *New J. Phys.* **12**, 035002.
Robinson, I. & Harder, R. (2009). *Nat. Mater.* **8**, 291–298.
Santoro, A. (1974). *Acta Cryst.* A**30**, 224–231.
Sarma, D. D., Topwal, D., Manju, U., Krishnakumar, S. R., Bertolo, M., La Rosa, S., Cautero, G., Koo, T. Y., Sharma, P. A., Cheong, S. W. & Fujimori, A. (2004). *Phys. Rev. Lett.* **93**, 097202.
Sayre, D. (1952). *Acta Cryst.* **5**, 843.
Thibault, P., Dierolf, M., Menzel, A., Bunk, O., David, C. & Pfeiffer, F. (2008). *Science*, **321**, 379–382.
Turner, J. J., Jordan-Sweet, J. L., Upton, M., Hill, J. P., Tokura, Y., Tomioka, Y. & Kevan, S. D. (2008). *Appl. Phys. Lett.* **92**, 131907.
Uehara, M., Mori, S., Chen, C. H. & Cheong, S. W. (1999). *Nature (London)*, **399**, 560–563.
Van Aken, B. B., Meetsma, A., Tomioka, Y., Tokura, Y. & Palstra, T. T. M. (2002). *Phys. Rev. B*, **66**, 224414.
Vartanyants, I. A., Robinson, I. K., McNulty, I., David, C., Wochner, P. & Tschentscher, Th. (2007). *J. Synchrotron Rad.* **14**, 453–470.
Wang, Y. & Liebermann, R. C. (1993). *Phys. Chem. Miner.* **20**, 147–158.
White, T. J., Segall, R. L., Barry, J. C. & Hutchison, J. L. (1985). *Acta Cryst.* B**41**, 93–98.
Yeates, T. O. (1997). *Methods Enzymol.* **276**, 344–358.